Supplementary Materials For

Shear-Related Gold Ores in the Wadi Hodein Shear Belt, South Eastern Desert of Egypt: Analysis of Remote Sensing, Field and Structural Data

Mohamed Abd El-Wahed, Basem Zoheir, Amin Beiranvand Pour * and Samir Kamh

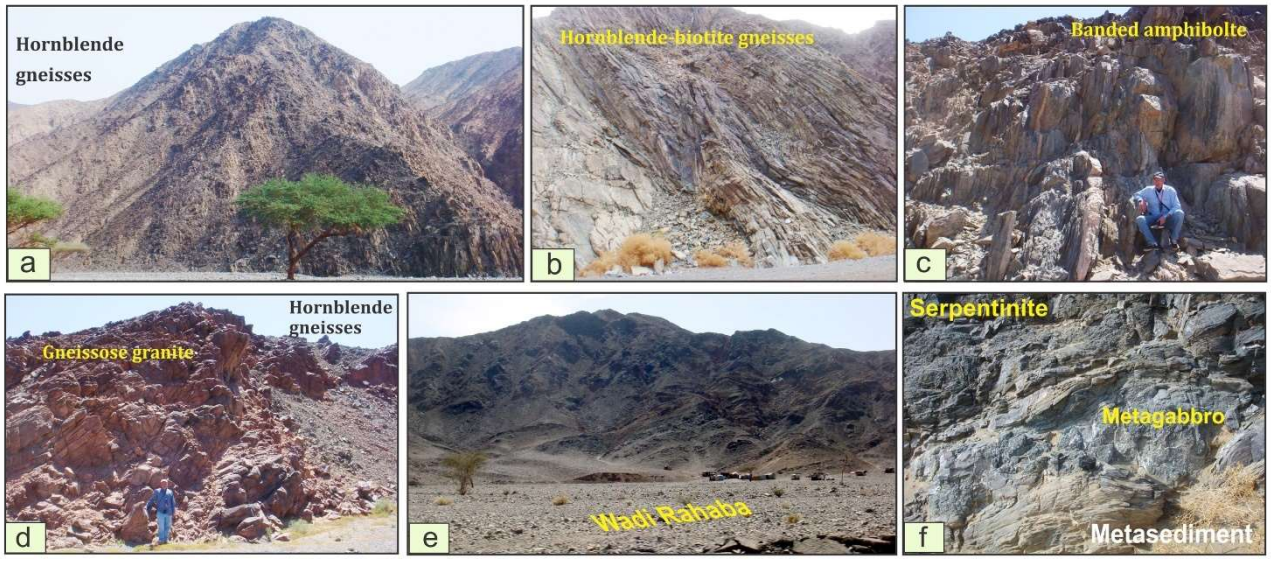

Figure S1. Field photographs showing the different rock units in the study area; (**a**) and (**b**) hornblende gneiss alternating with bands of biotite gneiss forming ENE-trending ridges along Wadi Khuda, (**c**) banded amphibolite from Beitan gneisses belt, (**d**) contact between hornblende gneisses and gneissose granite from Beitan gneisses belt (**e**) carbonated ophiolitic serpentinite enclosing small bodies of listivenitized ultramafites (dark ridges) from Wadi Rahaba, (**f**) small prophyroclast of ophiolitic metagabbro between volcaniclastic metasediment (lower) and serpentinite (upper) from Wadi Rahaba.

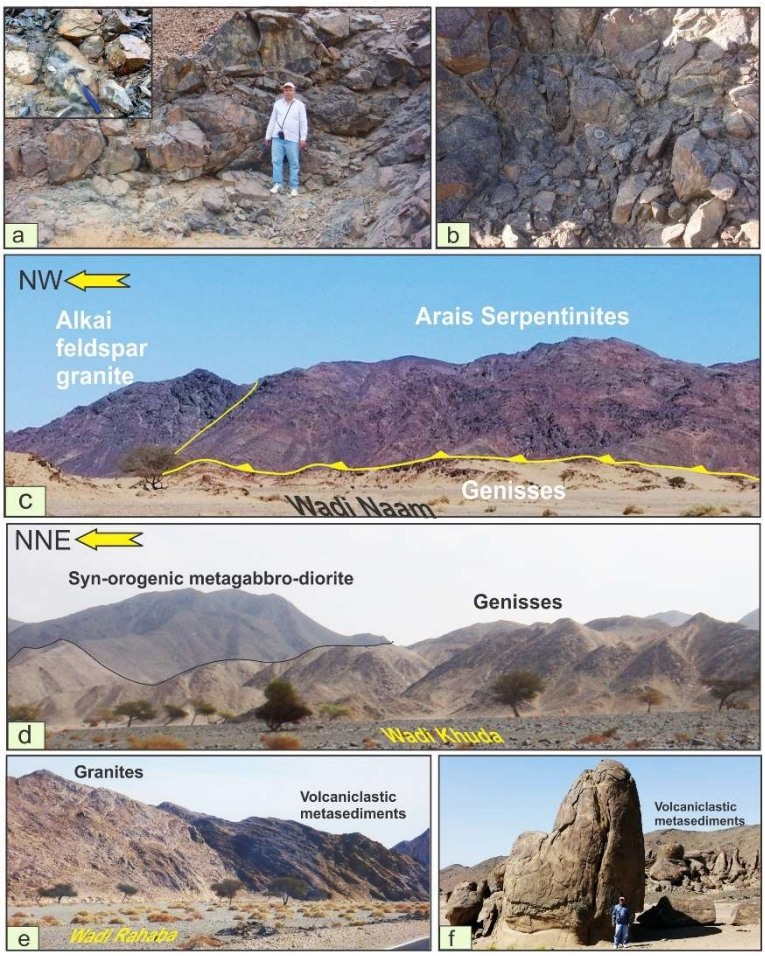

Figure S2. Field photographs showing the different rock units in the study area; (**a**) pillowed metabasalts from Wadi Khuda, northeast of Gabal Abu Dahr (**b**) ellipsoidal Pillowed metabasalt from Wadi Hutib, (**c**) serpentinized peridotites of Gabal Arais thrusted over the Beitan gneisses belt and are intruded by a small mass of alkali feldspar granite, (**d**) syn-orogneic gabbro-diorite intruded the gneisses of Wadi Khuda, (**e**) post orogenic biotite granite intrudes volcaniclastic metasediments along Wadi Rahaba, (**f**) syn-orogonic granodiorite intrudes volcaniclastic metasediments along Wadi Beitan.

Section S1. Data and Processing Techniques

Two cloud-free ASTER scenes 'AST_L1T00312252006082430 and 00312252006082422' were acquired on August 24, 2006. The Landsat-8 OLIL/TIRS scene 'LC08_L1TP1730442019073001_T1' was acquired on July 30, 2019 with path/raw 173/44. Four ALOS PALSAR scenes ALPSRP075090450, ALPSRP075090460, ALPSRP077570450 and ALPSRP077570460 of L-Band level 1.5 images. Landsat-8 OLI/TIRS and ASTER data is already geo-referenced to UTM (Universal Transverse Mercator), Zone 36 North with WGS-84 datum. The Internal Average Relative Reflection (IARR) method was applied for atmospheric correction of Landsat 8 OLI/TIRS and ASTER datasets. The IARR reflectance technique is a preferred calibration technique for mineralogical mapping in arid regions and requires no prior knowledge of samples collected from the field. Using the IARR, a reference spectrum is divided into each pixel in the image to generate relative reflectance [10]. Moreover, the 15 m-resolution ASTER VNIR bands have been resampled to match with the SWIR 30-m spatial dimensions and to correlate the 30-m resolution of the Landsat 8 OLI/TIRS. The layer staking, mosaicking and sub-setting of the used remotely sensed data were applied using the ENVI software, version 5.3, provided by Exelis Visual Information Solutions. The lithological contacts and structural elements were traced and delineated using the ArcGIS package software, version 10.5, provided by ESRI (Environmental Systems Research Institute, USA). ALOS PALSAR scenes are subjected to georeferencing

(UTM, Zone 36N) mosaicking, sub-setting and Enhanced Lee filter. Moreover, Principal Component Analysis (PCA) is applied to extract the lineaments automatically from PC1 image and lineaments density map and azimuth-frequency diagram are performed using PCI Geomatica and Rockworks softwares. These data have been processed for lithological mapping, highlighting structural elements and delineating the alteration zones. Image processing techniques, i.e., enhancement algorithms, band combinations (FCC), band math (BM), Principal Component Analysis (PCA), decorrelation stretch and mineralogical indices are applied for outlining geological mapping and the hydrothermal alteration zones in the study area. Finally, multi-criteria approach was applied to produce the potentiality gold mineralization map of the study area. Supplementary Figure 3 shows the flow chart of the methodology adopted for the present study.

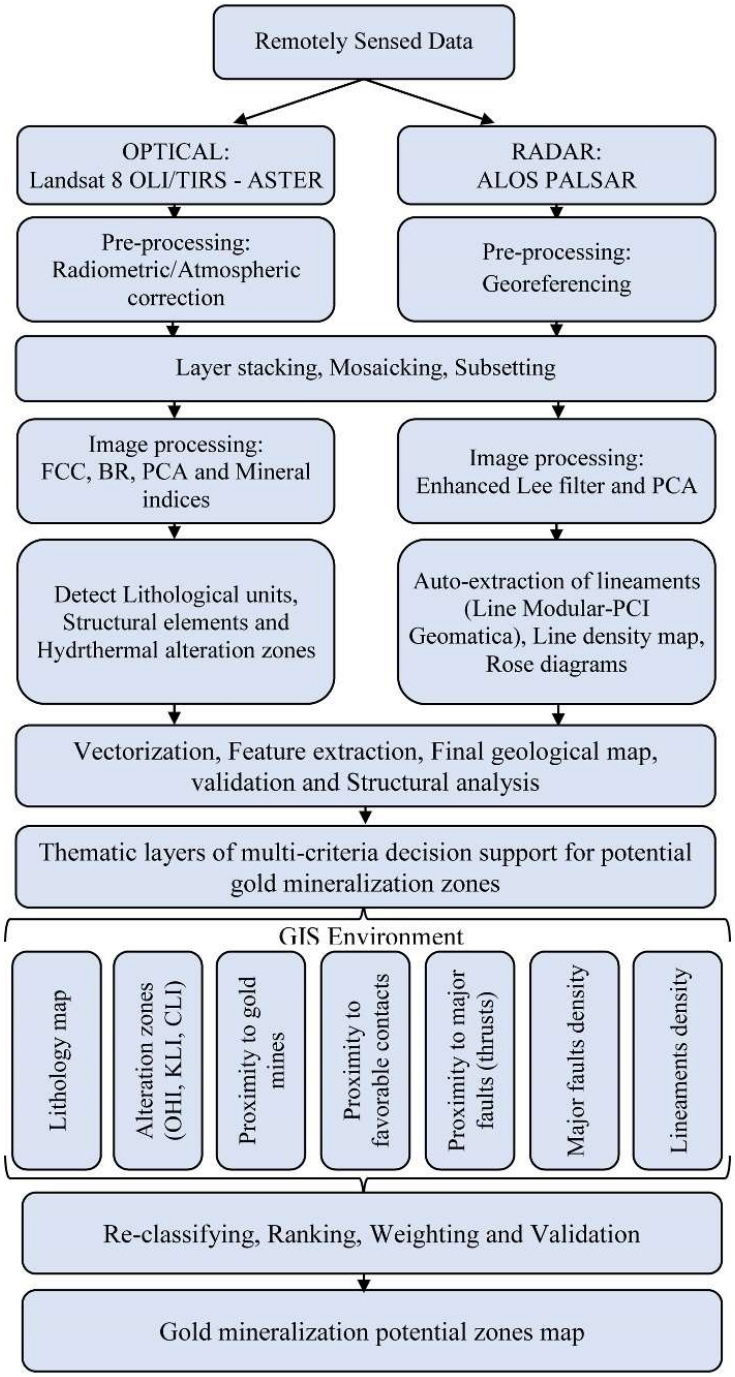

Figure S3. Flowchart of the remote sensing and GIS methodologies adopted in the present study.

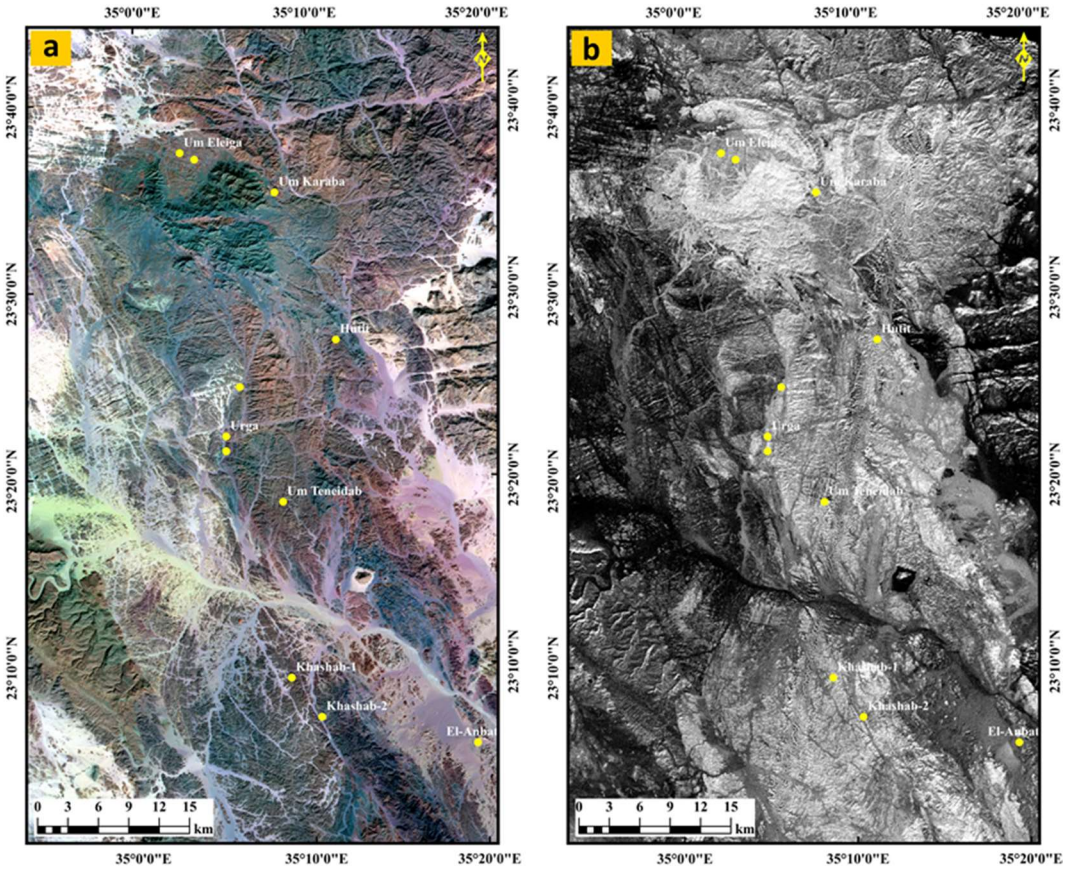

Figure S4. Lithological discrimination using (**a**) ASTER (RGB-431) and (**b**) Grey scale ASTER band ratio (7 + 9/8).

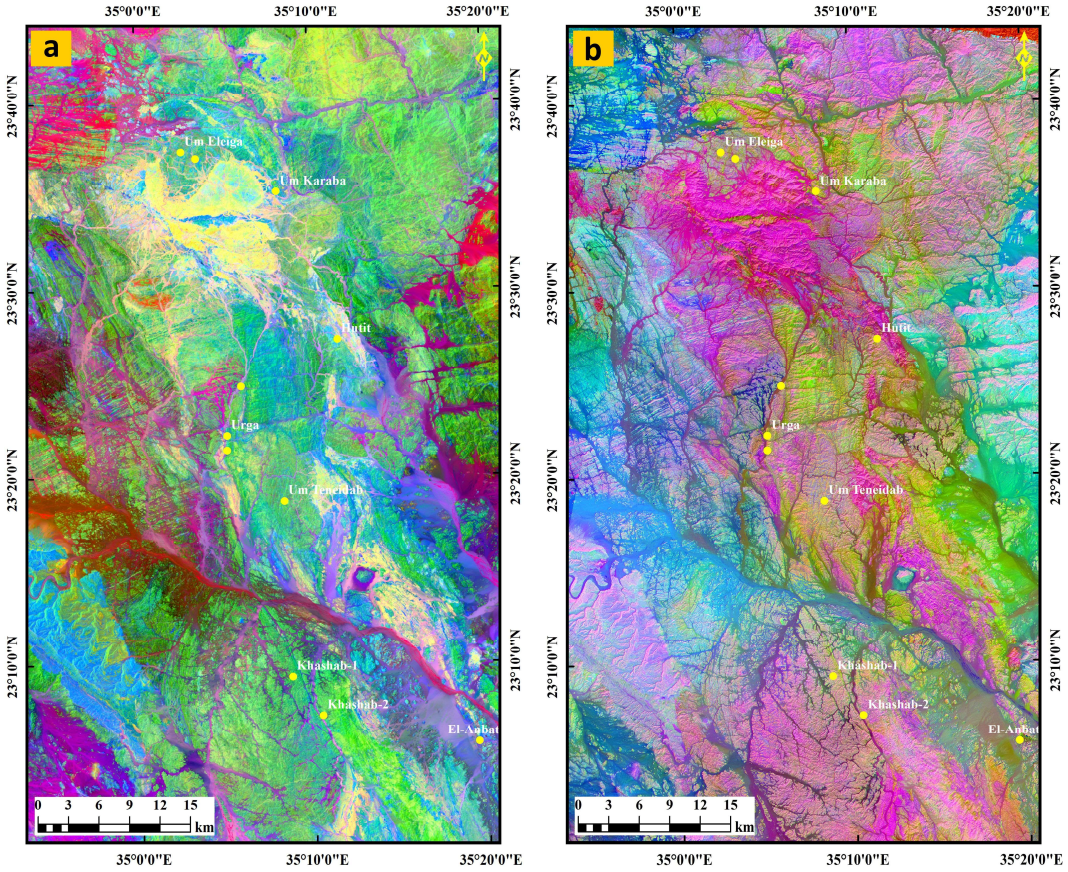

Figure S5. False-color composite of principal component analysis (PCA) of (**a**) Landsat-8 RGB-PC2, PC1, PC4 and (**b**) ASTER RGB-PC1, PC2, PC3.

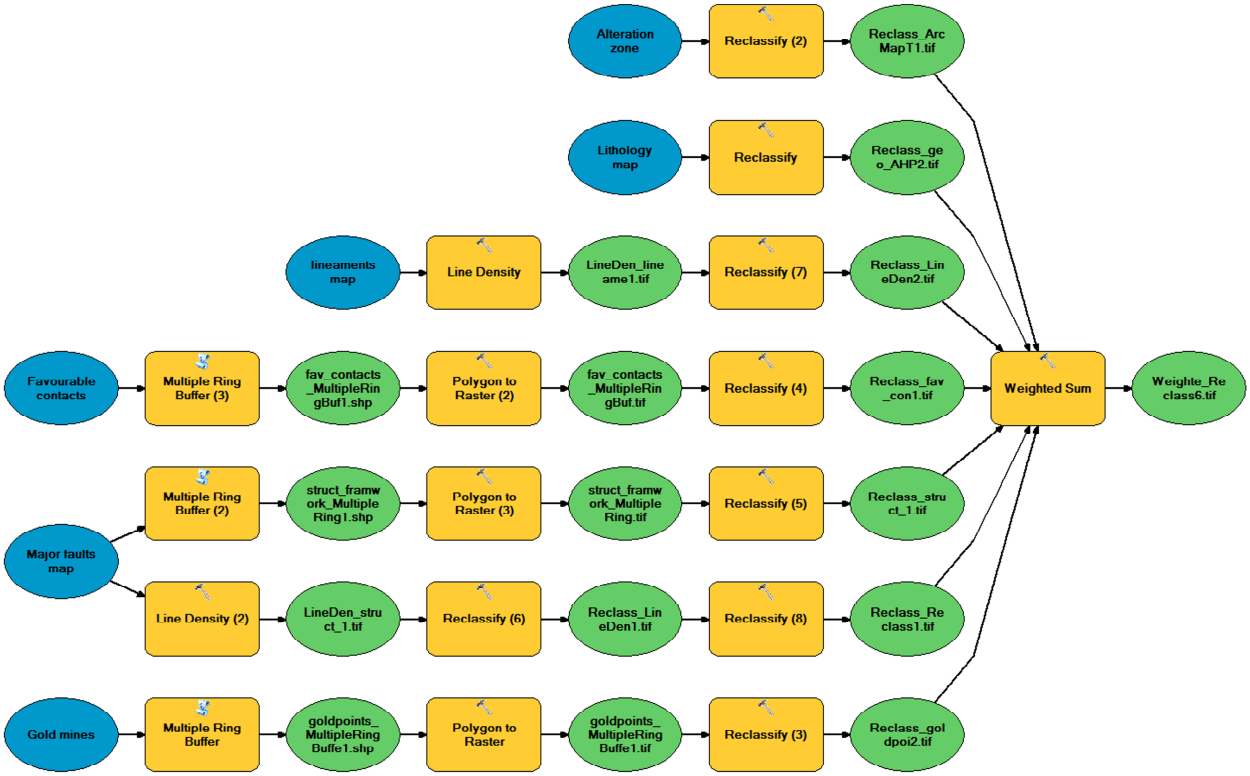

Figure S6. Model Builder of the geospatial thematic maps used to locate the high potential zones for gold mineralization in the study area.

Table S1. Eigenvector loadings of principal component analysis for Landsat-8 OLI data.

	PC1	PC2	PC3	PC4	PC5	PC6	PC7
Band 1	−0.105	−0.138	−0.234	−0.350	−0.448	−0.571	−0.516
Band 2	0.178	0.238	0.357	0.447	0.412	−0.341	−0.546
Band 3	−0.383	−0.444	−0.400	0.002	0.499	0.304	−0.393
Band 4	0.179	0.206	0.167	−0.094	−0.378	0.682	−0.530
Band 5	0.437	0.354	−0.229	−0.646	0.462	−0.017	−0.023
Band 6	−0.507	−0.023	0.693	−0.488	0.157	−0.009	0.001
Band 7	0.575	−0.747	0.312	−0.112	0.028	−0.004	−0.002

Table S2. Eigenvector loadings of principal component analysis for ASTER data.

	PC1	PC2	PC3	PC4	PC5	PC6	PC7	PC8	PC9
Band 1	−0.297	−0.359	−0.359	−0.339	−0.307	−0.330	−0.350	−0.354	−0.295
Band 2	−0.462	−0.492	−0.432	0.122	0.232	0.227	0.324	0.278	0.235
Band 3	−0.164	0.065	0.234	−0.489	−0.407	−0.366	0.339	0.413	0.299
Band 4	−0.243	−0.008	0.177	0.047	0.029	0.092	−0.797	0.364	0.360
Band 5	0.585	−0.013	−0.467	−0.534	0.128	0.218	−0.122	0.097	0.259
Band 6	−0.367	0.076	0.367	−0.548	0.337	0.418	0.058	−0.364	0.009
Band 7	−0.035	0.047	−0.006	−0.159	−0.114	0.353	−0.039	0.553	−0.725
Band 8	−0.029	0.044	−0.058	0.135	−0.734	0.588	0.042	−0.215	0.210
Band 9	−0.366	0.784	−0.493	0.009	0.057	−0.068	0.000	−0.003	0.026